Taguchi optimization of the peak lasing power of a numerically-simulated double wafer-fused InP/GaAs LW-VCSEL

P. S. MENON[a,*], P. R. APTE[b]

[a]Institute of Microengineering and Nanoelectronics (IMEN), Universiti Kebangsaan Malaysia (UKM)
43600 UKM Bangi, Selangor, Malaysia
[b]College of Engineering Pune, Pune - Maharashtra 411005, India

The advent of high speed and high bandwidth optical access networks, such as fiber-to-the-home (FTTH), is the driving force behind the demand for low-cost, high-power optical components. Long-wavelength Vertical Cavity Surface-Emitting Lasers (LW-VCSEL) are attractive as light sources in these networks because they offer unique features such as low power consumption, narrow beam divergence and ease of fabrication in two-dimensional arrays. Furthermore, device operation in the 1.55 µm wavelength regime offers the advantages of low dispersion and low optical loss in fiber optic transmission systems. This paper reports the optimization of the peak lasing power of a numerically simulated LW-VCSEL model which utilizes InGaAsP-based multi-quantum wells (MQW) using Taguchi's orthogonal array method in an effort to further increase the peak lasing power. Four control factors at three value levels form the inner L9 orthogonal array whereas two noise factors at three levels form the outer 3x3 factorial array. The optimum design parameter combination was obtained by using the analysis of 'larger-the-better' (LTB) and 'nominal-the-best' (NTB) signal-to-noise ratio (SNR). This work reports the fine-tuning of the factor levels to further increase the peak lasing power up to 12.62 mW which is a 160 % improvement compared to the original device design.

1. Introduction

The demand for low-cost, high-power and fast manufacturability of optical components such as the long-wavelength vertical-cavity surface-emitting lasers (LW-VCSEL) operating at 1.3 µm or 1.55 µm, is increasing rapidly in an attempt to meet the advent of high bandwidth and high speed optical networks especially in access networks such as fiber-to-the-home (FTTH) [1]. LW-VCSELs are favoured over the conventional edge-emitting-laser (EEL) and are used as light transmitters in transceivers of optical network units (ONU) and optical line terminals (OLT) in the FTTH system. They offer the advantages of low dispersion and low optical loss in fiber optic transmission systems which are crucial in increasing data transmission speed and in reducing the implementation cost of FTTH access networks. Some other unique features of LW-VCSELs include low power consumption, narrow beam divergence and ease of fabrication of devices in two-dimensional arrays [2].

LW-VCSELs operating in the 1.55 µm wavelength region have been fabricated using various fabrication techniques such as wafer fusion methodology [2-4], all epitaxial growth [5]-[8] and a combination of epitaxially-grown and dielectric distributed Bragg reflectors (DBRs) [9,10]. The aperture type in these devices consists of undercut quantum-wells, buried tunnel junctions (BTJ) or regrown tunnel junctions [11]-[12]. VCSEL devices developed using the wafer fusion method have achieved continuous wave (CW) operation above 100°C at 1.55 µm at a threshold current of 1 mA at 2.4 V voltage. The highest output power obtained at 20°C was 0.65 mW [3]. Implementation of the BTJ aperture type further increased the single-mode output power to 6 mW at room temperature [11]. The active region in the multi-quantum-well (MQW) layer of a LW-VCSEL is commonly developed using quartenary materials such as InGaAsP, InGaAlAs, AlInGaAs and GaInNAs [13-15]. The air-post wafer-fused LW-VCSEL is advantageous since there is enhanced thermal dissipation from the active region in both the lateral and vertical directions. Utilization of GaAs-based mirrors provides high reflectivity as well as thermal conductivity and Fig. 1 shows the schematic diagram of the selected double wafer-fused GaAs/InP-based LW-VCSEL.
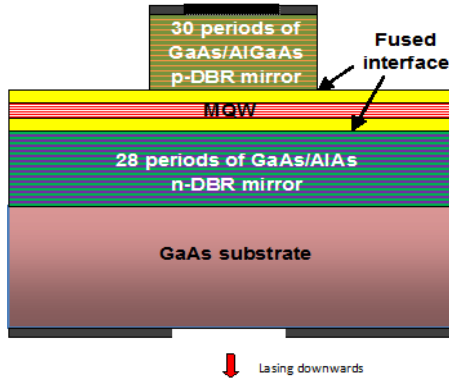
Fig. 1. Schematic diagram of the double wafer-fused GaAs/InP-based LW-VCSEL.

Design of experiment using Taguchi's orthogonal array (OA) methodology optimizes process parameters and results in robust device quality by making the output characteristics insensitive to variations in environmental conditions and other noise factors [16]. The Taguchi method is also used to perform the process of centering or fine-tuning where the central values of control factors are determined to achieve repeatable performance even when the levels of control factors have some variations around its central values [17]. Numerous works in the past have utilized the Taguchi method to optimize various product and process issues [18,19]. Else than Taguchi method, some other optimization methods are Response Surface Methodology (RSM) and Factorial Design; but these methods are complex and time consuming.

Physics based device simulators provide a more precise and comprehensive analysis and are much cheaper and quicker in providing comprehensive device performances as compared to a full laboratory prototype measurement. Device simulations using finite-element-method (FEM)-based simulators such as Silvaco's ATLAS [20,21] provide more insight into the various physical phenomenon and device characteristics by looking at trend plots over device structural parameters and probing into cross-section structures rather than the analytic model. Hence, the double wafer-fused GaAs/InP LW-VCSEL was developed using Silvaco's ATLAS using a modified design from the experimental device in the past [22,23].

This paper combines the usage of numerical modelling and simulations based on Taguchi OA to obtain the optimized and fine-tuned peak lasing power of a double wafer-fused GaAs/InP LW-VCSELs operating in the 1.55 µm wavelength region. To the author's knowledge, this is the first time Taguchi method is used to optimize and fine-tune the peak lasing power of a simulated LW-VCSEL model. Our previous work emphasized on the optimization of the peak lasing power using Taguchi's OA whereas in this paper we analyze the Taguchi's fine-tuning process in an attempt to further increase the peak lasing power.

2. Theoretical analysis for numerical modelling and simulation

The basis of the simulation is to solve two-dimensional Poisson's equation and the continuity equations for electrons and holes. Poisson's equation which is given by [20]

$$\nabla \bullet (\in \nabla \Psi) = \rho \tag{1}$$

which relate variations in electrostatic potential ψ to local charge densities ρ and the local permittivity ε. The continuity equations are given by [20]

$$\frac{\partial n}{\partial t} = G_n - R_n + \frac{1}{q}\nabla \cdot \vec{J}_n \tag{2}$$

$$\frac{\partial p}{\partial t} = G_p - R_p + \frac{1}{q}\nabla \cdot \vec{J}_p \tag{3}$$

where n and p are the electron and hole concentrations, J_n and J_p are the electron and hole current densities, G_n and G_p are the generation rates for electrons and holes, R_n and R_p are the recombination rates and q is the magnitude of the charge on an electron.

The basic semiconductor equations (1)-(3) are solved self-consistently together with the Helmholtz, lattice heat flow and the photon rate equations. Two-dimensional Helmholtz equation is solved to determine the transverse optical field profile using the effective frequency method (EFM) and it is given by [20]:

$$\nabla^2 E(r, z, \varphi) + \frac{\omega_0^2}{c^2} \varepsilon(r, z, \varphi, \omega) E(r, z, \varphi) = 0 \tag{4}$$

where ω is the frequency, $\varepsilon(r, z, \varphi, \omega)$ is the complex dielectric permittivity, $E(r, z, \varphi)$ is the optical electric field, and c is the speed of light in vacuum. The heat flow equation has the form [20]:

$$C\frac{\partial T_L}{\partial t} = \nabla(\kappa \nabla T_L) + H \tag{5}$$

where C is the heat capacitance per unit volume, κ is the thermal conductivity, H is the generation and T_L is the local lattice temperature. The photon rate equation is solved in order to obtain the modal photon density, S_m and is given by [20]:

$$\frac{dS_m}{dt} = \left(\frac{c}{N_{eff}}G_m - \frac{1}{\tau_{ph_m}} - \frac{cL}{N_{eff}}\right)S_m + R_{sp_m} \tag{6}$$

where G_m is the modal gain, R_{spm} is the modal spontaneous emission rate, L represents the losses in the laser, N_{eff} is the group effective refractive index, τ_{phm} is the modal photon lifetime and c is the speed of light in vacuum. Equations

(1)-(6) provide an approach that can account for the mutual dependence of electrical, optical and thermal phenomena in the development of a comprehensive VCSEL model.

The energy levels E_q of a particle of mass m confined to a one-dimensional infinite rectangular well of full width d are determined by solving the time-independent Schrodinger equation [30].

$$\mathbf{E_q} = \frac{\hbar(q\pi/d)^2}{2m} \qquad (7)$$

where $q=1,2,\ldots\ldots$. This means the smaller the width of the quantum well, the larger the separation between adjacent energy levels. The default energy band-gap for the InP lattice matched $In_{1-x}Ga_xAs_yP_{1-y}$ system used in this modelling is given by [20]:

$$E_g = 1.35 + (0.642 + 0.758x)x + (0.101y - 1.101)y - (0.28x - 0.109y + 0.159)xy \qquad (8)$$

where x and y are the respective mole fraction for the III-V material used as the MQW material. The peak lasing power, P_{01} of a VCSEL is defined as

$$P_{01} = F_1 \frac{hv}{q} \eta_D(I - I_{th}) \qquad (9)$$

where F_1 is the fraction of optical power that is emitted at DBR mirror 1, hv is the photon energy, I is the terminal current, I_{th} is the critical current and η_D is the differential efficiency. Fig. 2 shows the simulation domain of the LW-VCSEL in Silvaco [20].
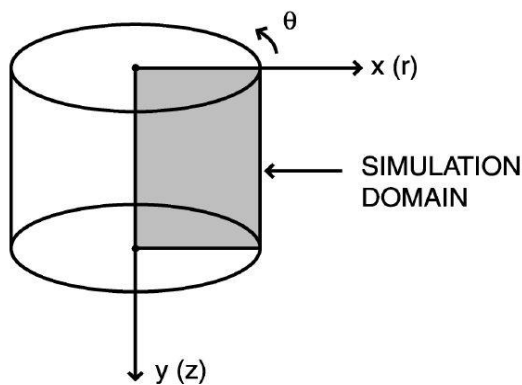
Fig. 2. The relationship between rectangular and cylindrical coordinate systems used by the VCSEL module.

3. Theoretical analysis for Taguchi's method

Signal-to-noise ratio (SNR, η) in Taguchi's method are log functions of the desired output which is being investigated. It transforms several repetitions into one value which is a useful improvement of quality through reducing the variability. There are three different types of SNR; smaller-the-better (STB), larger-the-better (LTB) and nominal-the-best (NTB). In this work, the peak lasing power, P_i is being optimized to achieve higher values hence LTB SNR is used and is given by the following equation [25]:

$$\eta_{LTB} = -10 \cdot \log_{10}\left[\frac{1}{n}\sum_{i=1}^{n}\frac{1}{P_i^2}\right] \qquad (10)$$

where P_1 is the peak lasing power and n is the number of simulation experiments. The LTB SNR given in equation (10) as derived by Taguchi [25], takes the normal logarithmic value of the mean reciprocal square of the output values, and is expressed in decibels (dB). The higher the SNR value, the better the performance of the device.

Upon optimization using the LTB SNR, the centering or fine tuning process is executed. Since the aim is to simultaneously maximize the peak power as well as to make it insensitive to the noise factors, the NTB SNR is used for studying effect of noise factors. A scaling factor needs to be found that can serve as an adjustment factor. The NTB SNR is given by [25]

$$\eta_{NTB} = 10 \cdot \log_{10}\frac{\mu^2}{\sigma^2} \qquad (11)$$

where the mean, $\mu = \frac{1}{n}\sum_{i=1}^{n}P_i$ and the variance, $\sigma^2 = \frac{1}{n-1}\sum_{i=1}^{n}(P_i - \mu)^2$. Another useful equation is the SNR for the mean value which is given by [25]

$$\eta_{Mean} = 10 \cdot \log_{10}\mu^2 \qquad (12)$$

Once the SNR values are obtained, factor effect plots can be constructed to show the effects of the respective control factors and their level values on the selected response. The factor effect plot as shown in Fig. 3 using the NTB SNR indicates the rate at which a particular control factor level affects the SNR i.e. the variance. Best settings that give the highest response are then selected (shown by the star) for each control factor. Each selected setting implies reduced variance.
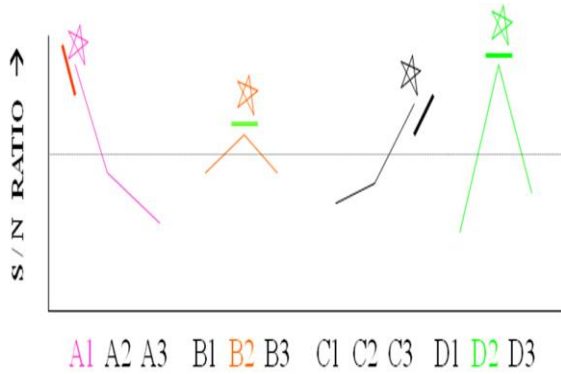
Fig. 3. Factor effect plot for NTB SNR. Best settings that give the highest response are then selected (shown by the star) for each control factor.

Similarly, the factor effect plot using the mean value, μ, indicates the rate at which a particular control factor level affects the mean (as indicated by the slope) as shown in Fig. 4. Once again the same best settings are selected (as shown by the star in Fig. 3) for each control factor level. Each selected setting implies reduced variance but could affect the mean significantly. From Fig. 4, the slope at control factor level A1 is large, slope at B2 is medium and finally the slope at C3 and D2 are small. Therefore control factor B has the smallest effect on the SNR but has a large effect on the mean. Hence, control factor B is an adjustment factor and can be used for adjusting the mean-on-target [25].
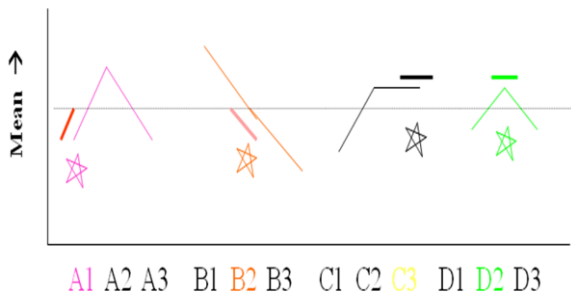
Fig. 4. Factor effect plot for SNR for the mean value. Best settings are shown with a star and thickened lines indicate slope. Control factor B is an adjustment factor because it has a small effect on SNR but a large effect on the mean.

4. Results of numerical modelling and characterization

Fig. 5 shows the simulated design [20] of the air-post double wafer-fused GaAs/InP-based 1.5 µm LW-VCSEL device modified from the experimental device in the past [22]-[23]. In this structure, the MQW active region consists of six 5.5-nm thick $In_{0.76}Ga_{0.24}As_{0.82}P_{0.18}$ quantum wells and 8-nm thick $In_{0.48}Ga_{0.52}As_{0.82}P_{0.18}$ barriers. The MQWs are embedded in InP spacer layers that have been extended by thin GaAs layers on top of each fused mirror to increase emission wavelength. Alternating high- and

low-refractive index layers of GaAs/$Al_{0.33}Ga_{0.67}As$ form the top 30-period p-type distributed Bragg reflector (DBR) whereas the bottom n-type DBR mirror is formed with 28-periods of GaAs/AlAs layers. The modelled nominal device achieved threshold current of 0.8 mA, output lasing power of 4.84 mW at a bias voltage of 3 V and optical wavelength of 1.56 µm. Fig. 6 shows the variation of the lasing power versus the electrical current when different quantities of MQWs are used.
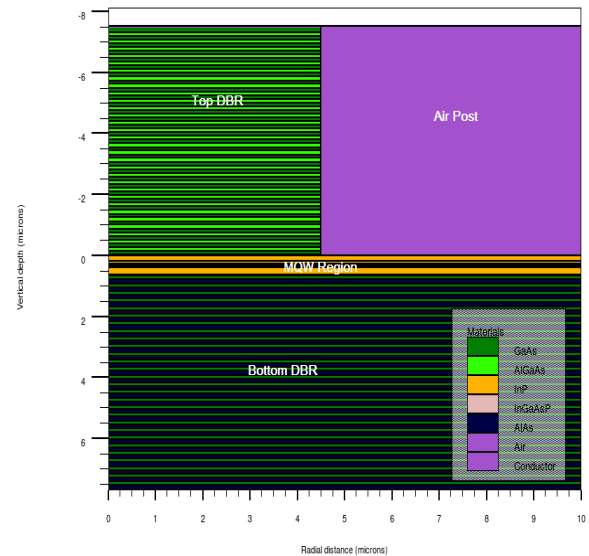
Fig. 5. Two dimensional view of the simulated GaAs/InP-based double wafer-fused LW-VCSEL.
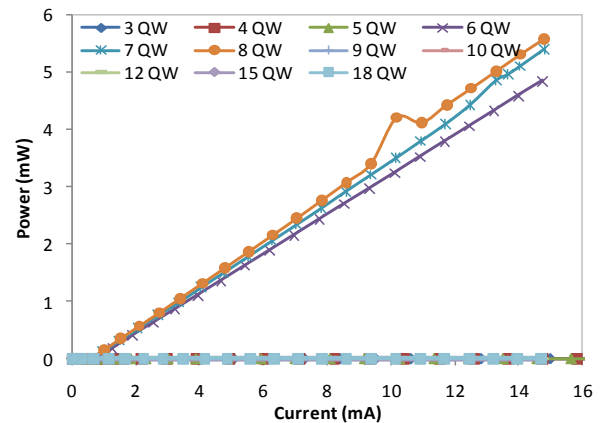
Fig. 6. Optical lasing power versus current curve (L-I) for different quantities of MQW.

5. Results of device optimization using Taguchi's method

Taguchi method was utilized to improve the peak lasing power by optimising the control and noise factor levels. Initially, four control factors namely MQW quantity, MQW thickness, x-component mole fraction in the MQW material and the dopant concentration in the top DBR mirror were chosen. Two noise factors which are the

device width and mesa pillar width were also selected. A schematic diagram of the device showing the selected control and noise factors is shown in Fig. 7.
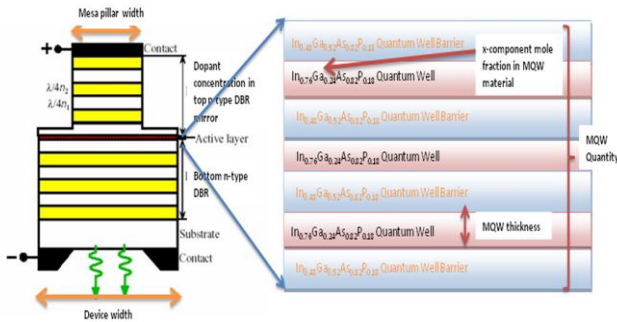
Fig. 7. Schematic diagram of both the double wafer-fused LW-VCSEL and a blown-up view of the MQW region showing the selected control and noise factors.

In our previous work [26-31], we used the control and noise factors with nominal level values (bold and underlined) as in Table 1. Initially, a L9 orthogonal array (OA) for four three-level control factors with three-level noise factors were used where a total of 81 experiments were used to optimize the LW-VCSEL peak lasing power. This was followed by a L4 OA which comprises of 3 two-level control factors and 2 three-level noise factors which consisted of 36 experiments. These two sets of optimization were able to increase the peak lasing power by 96.5 % from 4.84 mW to 9.51 mW at a bias voltage of 2 V and optical wavelength of 1.56 μm. The starting control/noise factor level combination of A2B2C2D1E1F1 is replaced with new optimized levels of A2B3C2D1E2F3 where the optimised level values are highlighted in Table 1 (with an asterick *). Details of the thorough optimization methodology and results for the peak lasing power can be obtained from our previous work [26]-[31].

Table 1. Control/Noise Factors and their level values. Initial values are bolded and underlined. Level values upon optimization are marked with an asterick (*).

Label	Control factors	Unit	Level 1	Level 2	Level 3
A	MQW Layers	-	4	6*	8
B	MQW thickness	nm	3.5	5.5	7.5*
C	x-component mole fraction in MQW material In(1-x)Ga(x)As(y)P (1-y)	-	0.14	0.24*	0.34
D	Dopant concentration in p-type top DBR mirror	cm^{-3}	4e17*	1e18	4e18

Label	Noise Factors	Unit	Level 1	Level 2	Level 3
E	Mesa pillar width	μm	6	8*	10
F	Device width	μm	12	15	18*
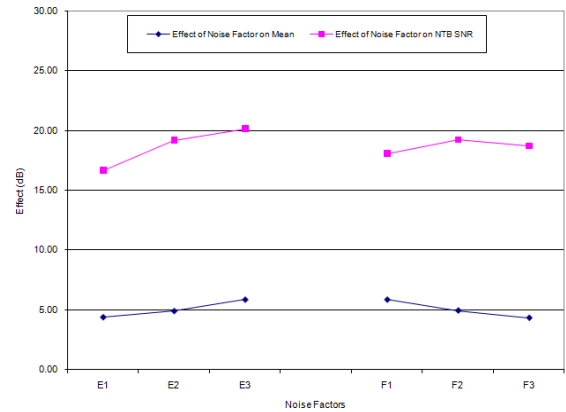
Fig. 8. Noise factor effect plot for both the NTB SNR and the SNR for the Mean.

6. Device Fine-tuning using Taguchi method

Next, the peak lasing power is fine tuned by taking the best settings of the control and noise factor levels from previous work [26]-[30] but with a reduced spread in the levels of control factors and noise factors. Table 2 list the new control and noise factor levels. Factor D is kept at a constant value of 4e17 cm^{-3} because it has the least effect on the optimization. Simulation experiments are conducted using a L9 OA for control factors and 9 combinations of the 2 noise factors at 3 levels each, leading to 9x9=81 simulation experiments. The results are showed in Table 3. The highest lasing powers were achieved for experiments 4, 6, 7 and 8.

Table 2. Control/Noise Factors and their level values for fine-tuning.

Label	Control factors	Unit	Level 1	Level 2	Level 3
A	MQW quantity	-	5	6	7
B	MQW thickness	nm	7	7.5	8
C	x-component mole fraction in MQW material In(1-x)Ga(x)As(y)P (1-y)	-	0.18	0.24	0.3

Label	Noise Factors	Unit	Level 1	Level 2	Level 3
E	Mesa pillar width	μm	7	8	9
F	Device width	μm	16	18	20

Table 3. Peak lasing power for fine-tuning experiments (mW).

Experiment No	1	2	3	4	5	6	7	8	9
1	0.00	0.00	0.00	0.00	0.00	0.00	0.00	0.00	0.00
2	0.00	0.00	0.01	0.00	0.01	0.00	0.01	0.00	0.00
3	0.01	0.01	0.01	0.01	0.01	0.01	0.01	0.01	0.01
4	6.95	9.02	11.32	7.32	9.47	6.50	7.27	8.53	10.74
5	0.00	0.00	0.00	0.00	0.00	0.19	0.00	0.00	0.04
6	6.98	9.09	11.39	6.98	6.98	11.10	7.33	8.56	10.85
7	7.56	9.85	12.38	7.55	9.79	6.98	0.00	8.79	11.78
8	7.68	10.01	11.91	7.69	9.95	4.66	7.65	9.45	11.96
9	0.00	0.00	0.00	0.00	0.00	0.00	0.00	0.00	0.00

Table 4 shows the factor effect SNR for the noise factors whereas Table 5 shows the factor effect SNR for the noise factors at each level upon fine tuning. These tables were derived from ANOVA calculations with Fisher Factor "F" > 2; equivalent to "% Effect" > 15% to identify the significant factors. Fig. 8 shows the factor effect plots for the NTB SNR and the SNR for mean for the noise factors E and F. The results show that the maximum SNR for the mean is obtained for noise combinations E3F3 (21.42 dB) and E3F2 (20.90 dB) implying that insensitivity is achieved for the noise factor F (Device Width) with values of F2=15 µm and F3=20 µm.

Table 4. Factor effect SNR for noise factors.

Quality Characteristic	E1F1 1	E2F2 2	E3F3 3	E1F2 4	E2F3 5	E3F1 6	E1F3 7	E2F1 8	E3F2 9	Overall Mean
Mean	7.21	9.39	11.78	7.29	9.13	8.04	5.90	8.76	11.08	
Variance	16.47	27.92	42.39	16.98	28.48	11.36	16.70	24.00	39.69	
NTB SNR (dB)	5.00	5.00	5.15	4.96	4.67	7.55	3.19	5.06	4.91	5.05
SNR for Mean (dB)	17.17	19.46	21.42	17.26	19.21	18.11	15.42	18.86	20.90	18.64

Table 5. Factor effect SNR for noise factors at each level.

Parameter	Noise Factor					
	E1	E2	E3	F1	F2	F3
Effect of Noise factor on SNR for Mean	4.38	4.91	5.87	5.87	4.95	4.34
Effect of Noise factor on NTB SNR	16.61	19.18	20.14	18.04	19.20	18.68

Table 6 shows the factor effect SNR for the control factors upon fine-tuning. Again, the results show that insensitivity is achieved for control factor C (mole fraction) with values of C2=0.24 and C3=0.3. The best settings are found for experiment #7 in Table 3 which has the following control and noise factor values, A3=7, B1=7 nm, C2=0.24, D=4e17 cm-3, E3=9 µm and F3=20 µm which contributes to a LTB SNR value of 21.63. As a result of the fine-tuning, the peak lasing power is increased up to 12.38 mW which is a 155 % improvement compared to the original device model.

Table 6. Factor effect SNR for control factors.

Experiment No	Control Factor Level Value			Noise factor SNR		Mean sum of reciprocals squared	LTB SNR (dB)
	A	B	C	E3F3	E3F2		
4	6	7	0.3	11.32	10.77	8.24E-03	20.84
6	6	8	0.24	11.39	10.85	8.10E-03	20.91
7	7	7	0.24	12.38	11.78	6.87E-03	21.63
8	7	7.5	0.3	11.92	11.96	7.02E-03	21.54
Mean				11.78	11.09		
Variance				42.39	39.70		

Further fine-tuning simulation experiments were carried out around the x-component mole fraction of 0.24 for the MQW material. Table 7 and Fig. 9 show results of the peak lasing power versus the x-mole component where as the x-mole component fraction is increased, the lasing power increases up to 12.62 mW until x_{QW}=0.34. Beyond this value, no lasing occurs when x_{QW} =0.35 onwards since the optical intensity profile within the device does not peak at the MQW region which is a pre-requisite factor for lasing to occur. Also, for x_{QW} <0.24, a change in the mole fraction causes the reflectivity of the top and bottom DBR mirrors to drop since the reflectivity is calculated from the optical intensity profile. This phenomenon is exhibited in Fig. 10 for the different mole fractions.

Table 7. Confirmation experiment for control factor C.

x-component mole fraction in MQW material In(1-x)Ga(x)As(y)P(1-y)	Peak lasing power (mW)	Quantum Well Energy bandgap, x=variable, y=0.82 (eV)	Quantum Well Barrier Energy bandgap, x=0.52, y=0.82 (eV)	Threshold current (mA)
0.2	No lasing	0.65	0.96	No lasing
0.21	12.31	0.66	0.96	0.94
0.22	No lasing	0.67	0.96	No lasing
0.23	No lasing	0.68	0.96	No lasing
0.24	12.38	0.69	0.96	0.75
0.25	12.40	0.69	0.96	0.67
0.26	12.42	0.70	0.96	0.62
0.27	12.44	0.71	0.96	0.57
0.28	12.47	0.72	0.96	0.53
0.29	12.49	0.73	0.96	0.48
0.30	12.51	0.74	0.96	0.44
0.31	12.54	0.75	0.96	0.40
0.32	12.56	0.76	0.96	0.35
0.33	12.59	0.77	0.96	0.31
0.34	12.62	0.78	0.96	0.29
0.35	No lasing	0.79	0.96	No lasing
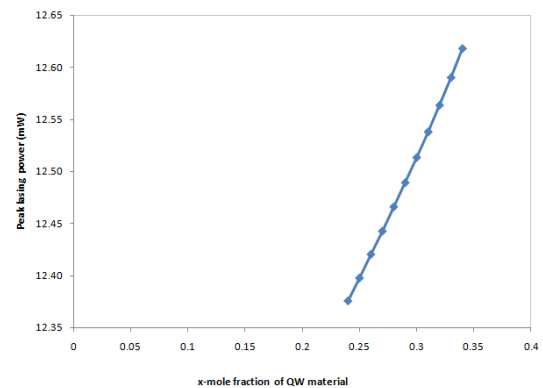
Fig. 9. Peak lasing power versus x-mole fraction of QW material.

Increment in the peak lasing power from a device physics perspective as a result of the Taguchi fine-tuning method is given as follows. Increment in the MQW layers and thickness increases the photon density which contributes to higher lasing powers. Increment in the x-component mole fraction increases the band gap energy of the MQW layers with respect to the band gap energy of the MQW barriers. Hence, mobile carrier flow between quantum wells is enhanced. Increment in carrier density rate increases the photon density rates as well as a higher number of recombination processes occur in the MQW region which contributes to the higher peak lasing power. Increment in the pillar width increases the total carrier density which is involved in the recombination process whereas increment in the device width increases the photon density and as a result higher lasing power is achieved.
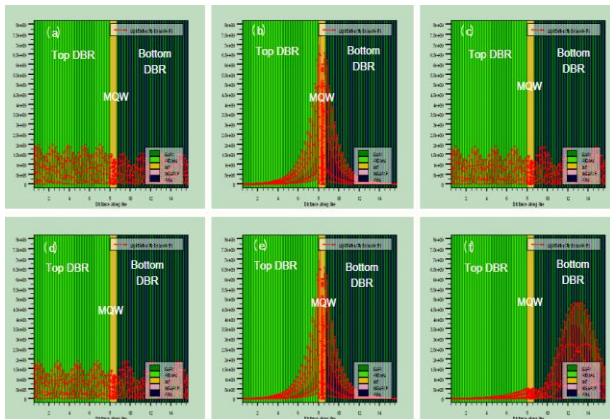
Fig. 10. Optical intensity profile within the LW-VCSEL structures where the $In_{1-x}Ga_xAs_yP_{1-y}$ MQW x-mole fraction is (a) 0.2, (b) 0.21, (c) 0.22, (d) 0.23 (e) 0.24 and (f) 0.35.

7. Conclusion

Double wafer-fused LW-VCSEL utilizing MQW active regions were developed, optimized and fine tuned using FEM-based numerical analysis and Taguchi's OA methodology namely the the LTB and NTB SNR. The original LW-VCSEL device model had a combination of initial control/noise factor levels of A=6, B=5.5 nm, C=0.14, D=4e17 cm^{-3}, E=6 µm and F=12 µm. The final optimised and fine tuned device had control/noise factor levels of A=7, B=7 nm, C=0.34, D=4e17 cm^{-3}, E=9 µm and F=20 µm. As a result of the new combination, insensitivity was achieved for control factor C and noise factor F where high lasing powers power were achieved.

Fine tuning of the factor levels increased the peak lasing power up to 12.38 mW which is a 155 % improvement compared to the original device. The highest peak lasing power of 12.62 mW was achieved for x-component mole fraction of MQW material of 0.34. Finally, an actual fabricated device using the above fine tuned parameters is required to confirm the increment in the peak lasing power. The fabrication of the optimized device will be attempted in the future.

References

[1] W. Hofmann, Semicond Sci Tech. **26**, 1 (2011).
[2] A. Karim, J. Piprek, P. Abraham, D. Lofgreen, Y.-J. Chiu, IEEE J. Sel. Topics Quantum Electron; **7**, 178 (2001).
[3] Y. Ohiso, H. Okamoto, R. Iga, K. Kishi, C. Amano, IEEE Photon. Technol. Lett. **14**, 738 (2002).
[4] A. V. Syrbu, V. P. Iakovlev, C. A. Berseth, O. Dehaese, A. Rudra, E. Kapon, J. Jacquet, J. Boucart, C. Stark, F. Gaborit, I. Sagnes, J. C. Harmand, R. Raj, Electron. Lett. **34**, 1744 (1998).
[5] W. Yuen, G. S. Li, R. F. Nabiev, J. Boucart, P. Kner, R. J. Stone, D. Zhang, M. Beaudoin, T. Zheng, C. He, K. Yu, M. Jansen, D. P. Worland, C. J. Chang-Hasnain, Electron. Lett. **36**, 1121 (2000).
[6] S. Nakagawa, E. Hall, G. Almuneau, J. K. Kim, D. A. Buell, H. Kroemer, L. A. Coldren, IEEE J. Sel. Topics Quantum Electron. **7**, 224 (2001).
[7] C. K. Lin, D. P. Bour, J. Zhu, W. H. Perez, M. H. Leary, A. Tandon, S. W. Corzine, M. R. T. Tan, IEEE J. Sel. Topics Quantum Electron. **9**, 1415 (2003).
[8] J. H. Shin, B. S. Yoo, W. S. Han, O. K. Kwon, Y. G. Ju, J. H. Lee, IEEE Photon. Technol. Lett. **14**, 1031 (2002).
[9] R. Shau, M. Ortsiefer, J. Rosskopf, G. Bohm, F. Kohler, M. C. Amann, Electron. Lett. **37**, 1295 (2001).
[10] N. Nishiyama, C. Caneau, G. Guryanov, X. S. Liu, M. Hu, C. E. Zah, Electron. Lett. **39**, 437 (2003).
[11] E. Kapon, A. Sirbu, Nature Photonics. **3**, 27 (2009).
[12] K. H. Rhew, S. C. Jeon, D. H. Lee, B.-S. Yoo, I. Yun, Microelectron. Rel. **49**, 42 (2009).
[13] W. Hofmann, M. C. Amann, IET Optoelectron. **2**, 134 (2008).
[14] M. Mehta, D. Feezell, D. A. Buell, A. W. Jackson, L. A. Coldren, J. E. Bowers, IEEE J. Sel. Topics Quantum Electron. **42**, 675 (2006).
[15] H. Riechert, A. Ramakrishnan, G. Steinle, Semicond Sci Technol. **17**, 892 (2002).
[16] U. Esme, Arabian J. Sc. Eng. **34**, 519 (2009).
[17] P. R. Apte, Why/When is Taguchi Method Appropriate?. WhyTaguchiMethod tip#10, http://www.ee.iitb.ac.in/~apte/WhyTaguchiMethodTip10.ppt. 2001
[18] C.-T. Su, C.-J. Yeh, Microelectron. Rel. **51**, 53 (2011).

[19] M. Y. Tsai, C. W. Ting, C. Y. Huang, Y.-S. Lai, Rel. **51**, 642 (2011).

[20] SILVACO International. ATLAS User's Manual. Version 5.16.3.R. Santa Clara CA USA; 2010

[21] Sona P. Kumar, Anju Agrawal, Rishu Chaujar, R. S. Gupta, Mridula Gupta, Microelectron. Rel. **51**, 587 (2011).

[22] N. M. Margalit, J. Piprek, S. Zhang, D. I. Babic, K. Streubel, R. P. Mirin, J. R. Wesselmann, J. E. Bowers, IEEE J. Sel. Topics Quantum Electron. **3**, 359 (2007).

[23] D. I. Babic, K. Streubel, R. P. Mirin, N. M. Margalit, J. E. Bowers, E. L. Hu, D. E. Mars, L. Yang, K. Carey, IEEE Photon. Tech. Lett. **7**(11), 1225 (1995).

[24] H. Li, K. Iga, Springer; 2002.

[25] M. S. Phadke, Quality engineering using robust design. Prentice-Hall; 2008.

[26] P. S. Menon, K. Kandiah, S. Shaari, J Nonlinear Optic Physics & Mat. **19**(2), 209 (2010).

[27] P. S. Menon, K. Kandiah, M. Ismail, B. Y. Majlis, S. Shaari, J Optic Comm. **31**, 81 (2010).

[28] P. S. Menon, K. Kandiah, M. Ismail, B. Y. Majlis, S. Shaari, Sains Malaysiana. **40**(6), 631 (2011).

[29] K. Kumarajah, P. S. Menon, M. Ismail, B. Y. Majlis, S. Shaari, WSEAS Trans. Electron. **11**(8), 437 (2008).

[30] P. S. Menon, K. Kandiah, B. Bais, H. Abdullah, B. Y. Majlis, P. R. Apte, In: Proc. of the 2010 IEEE Int Conf on Semicond Electron (ICSE2010): 365-369.

[31] K. Kandiah, P. S. Menon, S. Shaari, B. Y. Majlis, In: Proc. of the 2008 IEEE Int Conf on Semicond Electron (ICSE2008): 297-301.

_____
[*]Corresponding author: susi@ukm.edu.my